

Influence of Chemical Composition and Domain Morphology of Li_2MnO_3 on Battery Properties

Kazuhiro Hikima,^[a, b] Sou Taminato,^[c] Yoyo Hinuma,^[d] Keisuke Shimizu,^[d] Kota Suzuki,^[a, d] Masaaki Hirayama,^[a, d] Satoshi Yasuno,^[e] Kazuhisa Tamura,^[f] and Ryoji Kanno^{*[a, d]}

The reaction mechanism, which is the changes that happen during electrochemical cycling, in Li_2MnO_3 with a layered rock-salt ($\text{O}3$) structure was examined using model electrodes in a liquid battery. Epitaxial films of $\text{Li}_2\text{MnO}_3(001)$ with thickness of 30 nm, various Li/Mn atomic ratios, and different morphologies were fabricated by pulsed laser deposition. These electrodes showed charge-discharge capacity ranging from 150 to 300 mAh g^{-1} , with different degradation characteristics depending on the composition and morphology. Films with nominal (Li/Mn atomic ratio = 2.07) and Li-rich (Li/Mn ratio = 2.28) underwent irreversible structural transformation to an activated phase, regardless of the grain size, during the first cycling to

4.8 V. The interlayer spacing increased after activation, which may be a result of a transition to a $\text{O}1$ stacking structure. Li layer and transition metal layer octahedra share faces in the $\text{O}1$ structure, hence, Li diffusion would be easier and therefore results in activation considered to the $\text{O}1$ structure. Further degradation was slower in the nominal film, but the reason cannot be clearly ascribed to composition or grain size. *Ex situ* hard X-ray photoelectron spectroscopy (HAXPES) results suggest that some O were oxidized but others were not during charge. The Li-rich film showed large interactions with a solid-electrolyte interface layer by virtue of the high Li concentration.

1. Introduction

Layered rock-salt-type oxides capable of electrochemical intercalation and deintercalation of Li ions are widely used as cathode materials in current Li-ion batteries. Among these layered materials, the Li-rich oxide Li_2MnO_3 ^[1] shows the highest reversible capacity of 250–300 mAh g^{-1} , which exceeds the values of 150–220 mAh g^{-1} usually obtained for conventional materials such as LiCoO_2 and $\text{LiCo}_{1/3}\text{Ni}_{1/3}\text{Mn}_{1/3}\text{O}_2$.^[2,3] The large discharge capacity is reported to be caused by the formation of a high-capacity phase during the electrochemical activation

process, accompanied by Li and O extraction in the region of voltage plateau above 4.5 V versus Li/Li^+ during the initial charge cycle.^[4] Although an extremely large capacity is obtained, Li_2MnO_3 has many disadvantages: only nanometer-sized materials show large capacity; large capacity loss is observed at the first discharge cycle; the cell provides low current density for the charge-discharge reactions, which might be related to its insulating nature. To make high-capacity Li-rich layered oxide cathodes suitable for practical use, it is necessary to elucidate the reaction mechanism of these materials.

The activation mechanisms of such cathodes have been extensively investigated in liquid batteries in the past decade. The mechanisms that have been proposed so far are based on the structural changes and charge-compensation reactions that proceed in the plateau region with voltage above 4.5 V. Some of the proposed mechanisms are as follows: (1) the Mn ions remain in the tetravalent state during the oxidation reactions owing to the instability of pentavalent 3d transition metals at the six-coordinate octahedral positions;^[5] (2) oxidation is caused by O loss from the crystal lattice;^[4a] (3) the reaction of ion exchange between Li^+ and H^+ is accompanied by oxidation of the electrolyte solution;^[6] (4) Li_2O extraction through Li_2MnO_3 produces MnO_2 , which delivers electrochemical capacity during subsequent charge-discharge processes;^[6a,7] (5) oxide ions constituting the framework structure play a role in charge compensation during oxidation without O loss.^[8]

Various methods have been employed to synthesize Li_2MnO_3 as an electrode material, such as conventional solid-state reaction, hydrothermal techniques, and sol-gel process; even though they produce Li_2MnO_3 of similar particle size, different results have been obtained for the reversible capacity

[a] Dr. K. Hikima, Dr. K. Suzuki, Prof. M. Hirayama, Prof. R. Kanno
Department of Chemical Science and Engineering
School of Materials and Chemical Technology
Tokyo Institute of Technology
4259 Nagatsuta, Midori-ku, Yokohama 226-8502, Japan

[b] Dr. K. Hikima
Department of Electrical and Electronic Information Engineering
Tohohashi University of Technology
1-1 Hibarigaoka, Tempaku, Toyohashi, Aichi 441-8580, Japan

[c] Dr. S. Taminato
Department of Chemistry for Materials
Mie university
1577 Kurayamachiya-cho, Tsu, Mie 514-8507 Japan

[d] Dr. Y. Hinuma, Dr. K. Shimizu, Dr. K. Suzuki, Prof. M. Hirayama,
Prof. R. Kanno
All-Solid-State Battery Unit, Institute of Innovative Research
Tokyo Institute of Technology
4259 Nagatsuta, Midori-ku, Yokohama 226-8503, Japan

[e] Dr. S. Yasuno
Japan Synchrotron Radiation Research Institute (JASRI)
1-1-1 Koto, Sayo, Hyogo 679-5198, Japan

[f] Dr. K. Tamura
Quantum Beam Science Center
Japan Atomic Energy Agency
1-1-1, Koto, Sayo, Hyogo 679-5148, Japan

and cycle stability of Li_2MnO_3 electrodes.^[9] Their electrode properties can be affected by a deviation from the stoichiometric composition or differences in morphology with variations in the synthesis conditions. To understand the reaction mechanism, it is necessary to clarify the effects of the chemical composition and morphology on the activation reaction of a Li_2MnO_3 electrode.

Epitaxial-film electrodes provide a suitable model to analyze the reaction mechanism. The two-dimensional interface, which is free of binders and conductive additives, provides a simple reaction field.^[10] We previously studied the electrode characteristics of Li_2MnO_3 using a model of an epitaxial electrode with (001) orientation.^[11] Thinner epitaxial films exhibited higher reversible capacity, and the 12.6 nm-thick electrode provided a maximum capacity of $> 300 \text{ mAh g}^{-1}$ with high cycling stability. Although a high reversible capacity was obtained for the epitaxial Li_2MnO_3 model, the reaction mechanism remained unclear.

The present study elucidated the reaction mechanism of the epitaxial Li_2MnO_3 model electrodes synthesized using pulsed laser deposition (PLD) under different O pressures. Various synthesis conditions yielded epitaxial films with different compositions and morphologies, and their charge–discharge properties and structural changes during the first activation process were characterized by *in situ* X-ray diffraction (XRD) and *ex situ* hard X-ray photoelectron spectroscopy (HAXPES) measurements.

Experimental Section

Thin-Film Synthesis

The epitaxial $\text{Li}_2\text{MnO}_3(001)/\text{SrRuO}_3(111)$ films for this study were synthesized using a PLD system consisting of a 248 nm KrF excimer laser (COMPex201, Lambda Physik/Coherent, USA) and a vacuum chamber (PLD, PSAD-3000, AOV, Japan). Nb-doped (0.5 wt%) SrTiO_3 (111) and $\text{Al}_2\text{O}_3(001)$ single crystals ($10 \times 10 \times 0.5 \text{ mm}^3$, Crystal Base, Japan) were used as the substrates. Prior to deposition of each Li_2MnO_3 film, a SrRuO_3 film was prepared on a substrate as the current collector.^[12] The composition of the Li_2MnO_3 films was controlled to obtain the target composition and by varying the O pressure. Sintered pellets (diameter 20 mm \times 3 mm, Toshima Manufacturing, Japan) with the target compositions of $\text{Li}_{2.1}\text{MnO}_3$ (5% excess Li) and $\text{Li}_{2.4}\text{MnO}_3$ (20% excess Li) were used. The synthesis conditions of the Li_2MnO_3 films were as follows: substrate temperature of 973 K, target to substrate distance of 60 mm, laser frequency of 3 or 5 Hz, deposition duration of 10 or 20 min; laser energy of 1.1 J cm^{-2} , O pressure of 50 or 75 Pa, and post-deposition annealing at 673 K for 90 min in an infrared furnace.^[11] Table 1 summarizes the synthesis conditions used in the study.

Table 1. Conditions for synthesis of epitaxial Li_2MnO_3 films on a $\text{SrRuO}_3/\text{SrTiO}_3$ (111) substrate.

Sample	Frequency, f [Hz]	Deposition time, t [min]	Target composition	PO_2 pressure, P [Pa]	Post-deposition annealing
Li-poor	5	20	$\text{Li}_{2.1}\text{MnO}_3$	50	No
Nominal	3	10	$\text{Li}_{2.4}\text{MnO}_3$	75	Yes
Li-rich	3	10	$\text{Li}_{2.4}\text{MnO}_3$	75	No

Thin-Film Characterization

The crystal orientation of the thin films was characterized by out-of-plane and in-plane XRD measurements using thin-film X-ray diffractometers with $\text{CuK}_{\alpha 1}$ and MoK_{α} radiations (ATX-G and Smartlab, Rigaku, Japan). The thickness, density, and roughness of the films were determined by X-ray reflectivity (XRR) measurements using an X-ray diffractometer (ATX-G, Rigaku, Japan). The diffraction angles of the XRD data were calibrated with diffraction peaks of the SrTiO_3 substrate ($a = 3.905 \text{ \AA}$).^[13] The Parratt32 program was used for XRR analysis.^[14] The surface morphology of the films was investigated by atomic force microscopy (AFM; Nanoscope IV, Digital Instruments/Veeco, USA) and transmission electron microscopy (TEM; JEM-2010, JEOL, Japan). The Li and Mn concentrations (at%) in each sample were determined using inductively coupled plasma mass spectrometry (ICP-MS; 7500cs, Agilent Technologies, USA) after the thin film was dissolved in *aqua regia* diluted with ultrapure water at 373 K for 30 min. The valence state of Mn in the pristine samples was identified by HAXPES using the beamline BL46XU at the SPring-8 facility in Japan.

Electrochemical Measurements

The charge and discharge characteristics were examined using 2032-type coin cells assembled in an argon-filled glovebox. Each cell consisted of a Li metal anode and 1 mol dm^{-3} LiPF_6 in a mixture of ethylene carbonate (EC) and diethyl carbonate (DEC) (3:7, v/v) as the electrolyte (Kishida Chemical, Japan). The galvanostatic charge–discharge measurements were carried out at a current density of 5.16 A/g , in the voltage range of 2.0–4.8 V (vs. Li/Li⁺), and in the constant current (CC) mode. The charge and discharge capacities were calculated based on the deposited film area ($10 \times 7 \text{ mm}^2$), the thickness of the Li_2MnO_3 film determined by XRR analysis, and the theoretical density of Li_2MnO_3 .

In Situ XRD Measurements

The changes in the crystal structure of the films during electrochemical reactions were investigated by *in situ* surface XRD analysis using a spectro-electrochemical cell.^[10a] The counter electrode of the cell was made of Li metal, and the electrolyte solution consisted of a EC-DEC (3:7) mixture containing 1 mol dm^{-3} LiPF_6 . The XRD pattern of the $\text{Li}_2\text{MnO}_3(001)$ film was collected using a κ -type six-circle diffractometer (Newport Corporation, USA) installed at the bending-magnet beamline BL14B1 of the synchrotron beam facilities SPring-8 in Japan. The details of the experimental conditions are described elsewhere.^[16] The X-rays were monochromatized using a Si(111) double-crystal system and focused via two Rh-coated bent mirrors. An X-ray wavelength of 0.82518 \AA (15 keV) was employed. The measurements were performed using a reciprocal coordinate system (h , k , l) with two components (h and k) parallel to the surface and the third component (l) normal to the surface.^[15] De-intercalation and intercalation were induced using a potentiostat (Iviumstat, Ivium Technologies, The Netherlands). The XRD data were recorded for the pristine sample after the cell construction (OCV), at 4.4 and 4.8 V (vs. Li/Li⁺) after charging, and at 3.0 and 2.0 V after discharging.

Table 2. Parameters obtained by X-ray reflectivity analysis of Li_2MnO_3 films.

Sample	Surface layer Density, ρ [g cm $^{-3}$]	Thickness, t [nm]	Roughness, r [nm]	Li_2MnO_3 Density, ρ [g cm $^{-3}$]	Thickness, t [nm]	Roughness, r [nm]	SrTiO_3 Density, ρ [g cm $^{-3}$]	Roughness, r [nm]
Li-poor	2.33	2.93	1.6	3.92	25.0	1.7	5.15	3.5
Nominal	2.11	2.50	6.0	3.77	26.8	2.4	5.15	1.3
Li-rich	2.09	2.22	4.5	3.63	30.8	1.6	5.15	0.7

HAXPES Measurements

The chemical-bonding states of Mn and O were determined from Mn 3 s and O 1 s core-level HAXPES spectra acquired at SPring-8 BL46XU using a hemispherical electron energy analyzer (R-4000, Scienta Omicron, Germany) with an incident photon energy level of approximately 7940 eV. The binding energy was calibrated according to the C 1 s core-level spectrum (285 eV). The binding energy, linewidth, and integrated intensity of all measured core levels were determined through the standard fitting procedure using CasaXPS software (Version 2.3.17, Casa Software, UK). All core-level peaks were fitted to the Voigt function, which is a convolution of Lorentzian and Gaussian components. The Shirley background profile was used to fit the background spectra.^[16] The spectra of the as-prepared, charged (4.8 V in the first cycle), and discharged (2.0 V in the first cycle) samples were corrected at a take-off angle (TOA) of 80°. The escape depth of photoelectrons was ~30 nm,^[16] which corresponds to the bulk-enhanced information on electronic structures for penetrating the solid-electrolyte interphase (SEI) layer on the Li_2MnO_3 cathode film. Charged and discharged samples were prepared after the cells were cycled in the CC charge and discharge mode, followed by cycling in the constant-voltage (CV) mode for 1 h in an argon-filled glove box. After each cycle of charge–discharge measurements, the cells were disassembled immediately and rinsed in a dimethyl carbonate (DMC) solution. The samples were placed on the sample holder in the argon-filled glove box and carefully transported to the vacuum chamber without exposure to air or moisture.

2. Results

2.1. Characterization of Epitaxial Li_2MnO_3 Films

Figure 1 shows a schematic drawing of a Li_2MnO_3 film deposited on a $\text{SrRuO}_3/\text{SrTiO}_3(111)$ substrate. Table 2 summarizes the thickness, density, and roughness of the epitaxial films. The Li/Mn ratios of 1.75, 2.07, and 2.28 were determined by ICP-MS analysis (the film with Li/Mn ratio of 1.75 was evaluated by additional XRD, XRR, and HAXPES analyses in a previous study).^[17] These films are hereon denoted as Li-poor (Li/Mn = 1.75), nominal (Li/Mn = 2.07), and Li-rich (Li/Mn = 2.28) films.

All the films synthesized in this study had (001) and (010) orientations along the normal and (110) directions of the (111) substrate, as shown in the XRD and X-ray reflectometry (XRR) patterns (Figure 2). These diffraction peaks can be indexed by the space group $C2/m$.^[18] The diffraction peak around 20° corresponding to the 020 reflection is a characteristic of the interlayer ordering of Li and Mn ions in a honeycomb lattice. The lattice parameters of the films were slightly different from those of previously reported Li_2MnO_3 polycrystalline powder ($a=4.9246(1)$ Å, $b=8.5216(1)$ Å, $c=5.0245(1)$ Å, and $\beta=109.398(1)$ °).^[19] The expansion of the Li_2MnO_3 lattice along the a and b axes and the contraction along the c axis indicates that the lattices of all the Li_2MnO_3 epitaxial films were slightly distorted because of the lattice mismatch (2.1%) between the thin films and their respective $\text{SrRuO}_3/\text{SrTiO}_3(111)$ substrates. The thickness was 25.0, 26.8, and 30.8 nm, with surface roughness of 1.7, 2.4, and 1.6 nm for Li-poor, nominal, and Li-rich films, respectively. A surface layer with a density (ρ) of about 2.1 g cm $^{-3}$ was detected, indicating the formation of impurity phases such as Li_2CO_3 ($\rho=2.1$ g cm $^{-3}$) due to reactions of the films with moisture and carbon dioxide in air.

Figure 3 shows the AFM images of the nominal and Li-rich films. Among AFM, TEM, and SEM, AFM is the only method that can show, in a meaningful manner, the domain sizes of both nominal and Li-rich films. The former had a dense structure with large kinks (about 250 nm, large domain size) on the surface, while the latter showed low density structures with small kinks (about 20 nm, small domain size) on the surface. The domain size of the Li-poor film was about 5 nm based on TEM observations.^[17]

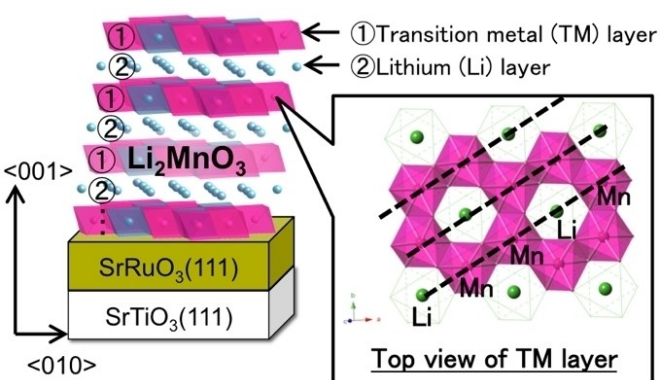


Figure 1. Crystal orientation and structural characteristics of Li_2MnO_3 film prepared on $\text{SrRuO}_3/\text{SrTiO}_3(111)$ substrate.

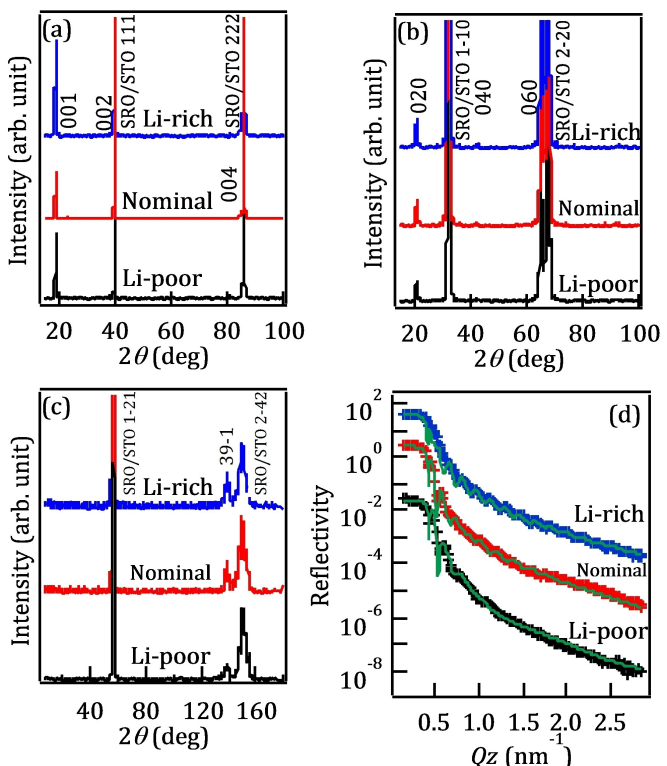


Figure 2. X-ray diffraction patterns of $\text{Li}_x\text{Mn}_y\text{O}_{3-z}$ (001) film electrodes synthesized on $\text{SrRuO}_3/\text{SrTiO}_3$ (111) substrate. The Li/Mn ratio was 1.75, 2.07, and 2.28 for Li-poor, nominal, and Li-rich films, respectively. a) $20/\omega$ scan along the [111] direction of SrTiO_3 (111) substrate; b) $20/\chi/\phi$ scan along the [110] direction of SrTiO_3 (111); c) $20/\chi/\phi$ scan along the [121] direction of SrTiO_3 (111). d) X-ray reflectivity and simulated curves of Li_2MnO_3 films.

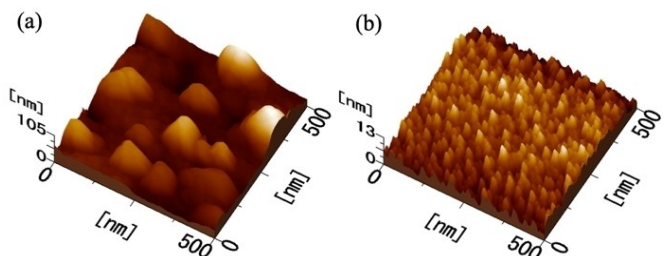


Figure 3. AFM images of the a) nominal and b) Li-rich $\text{Li}_x\text{Mn}_y\text{O}_{3-z}$ films synthesized on a $\text{SrRuO}_3/\text{SrTiO}_3$ (111) substrate.

2.2. Electrochemical Properties

Figure 4 shows the cycle dependence of the discharge capacities normalized by first discharge capacity, the average reaction voltage, charge-discharge curves, and the cycle dependence of the specific discharge capacities.^[17,20] Although the Li-poor and Li-rich films showed large first discharge capacities, these capacities decreased gradually with cycling.^[25,30] On the other hand, the discharge capacity of the nominal film increased continuously with cycling from the first cycle to the fifth cycle. This indicated that the activation to a high-capacity phase was completed after the first cycle for the Li-poor and Li-rich films, whereas the activation of the nominal

film continued with further cycling. Moreover, no significant capacity fading was observed for the nominal film; the average reaction voltage, which is the voltage at the half of the maximum discharge capacity at each cycle, was 3.1 V over the subsequent 80 cycles. The discharge capacity tended to decrease over 50 cycles in the Li-poor and Li-rich films, and a decrease in the discharge voltage was also observed for the Li-rich film. We previously reported the charge-discharge characteristics of Li_2MnO_3 films deposited on an Al_2O_3 (0001) substrate^[21] (denoted here as “previous Li_2MnO_3 film”). This previous Li_2MnO_3 film had a small (20 nm) domain size and showed large first discharge capacities with severe cycling capacity fading, which is similar to the Li-rich film in this study (20 nm domain size). Therefore, the severe capacity fading, which was found in the previous Li_2MnO_3 film and Li-rich film but not in the nominal film with large (~250 nm) domain size, is a characteristic of small domain size rather than the composition.

2.3. Crystal Structural Changes of Li_2MnO_3 Thin Film During Battery Operation

The crystal structural changes of Li_2MnO_3 thin film during battery operation were investigated for nominal and Li-rich films in which a single phase was observed. The Li-poor film was not investigated further because a second $\text{Li}_4\text{Mn}_5\text{O}_{12}$ spinel phase was found (see section 3.4.2 for details).

2.3.1. Nominal Film with $\text{Li}/\text{Mn}=2.07$ and Large Domain Size (250 nm)

Figures 5a and 5b show the 001 and $\bar{2}02$ peaks in the out-of-plane XRD patterns of the nominal film in the pristine state (Dry), after cell construction (OCV), after the first charge at 4.8 V, after the first discharge to 2.0 V, and during subsequent cycles. The 001 peak shifted to a lower d value from 4.724 Å in the OCV pattern to 4.701 Å in the pattern obtained after the first charge at 4.8 V, with a decrease in the intensity. During the first discharge from 4.8 to 2.0 V, the 001 peak shifted to a higher d value, from 4.701 to 4.779 Å, which was larger than that of the initial peak position ($d=4.724$ Å). A similar behavior was observed for the $\bar{2}02$ peak, which shifted from $d=1.924$ to 1.927 Å and then to 1.916 Å with the voltage change from that OCV to 4.8 V and then to 2.0 V. The peak intensity of the $\bar{2}02$ peak also decreased after the charge to 4.8 V. These peak shifts indicate that the structure at 2.0 V might have been different from the original O3-type structure because the lattice size should have remained the same if the Li had intercalated to their original composition in the O3 structure, which was observed for LiCoO_2 and LiNiO_2 .^[22] The peak after the second charge to 4.8 V was located at a d value (4.653 Å) lower than that after the first charge ($d=4.724$ Å), which indicates that the activation process was not completed in the first cycle and continued after the second cycle. This result is consistent with the electrochemical cycling result in Figure 4, which suggests

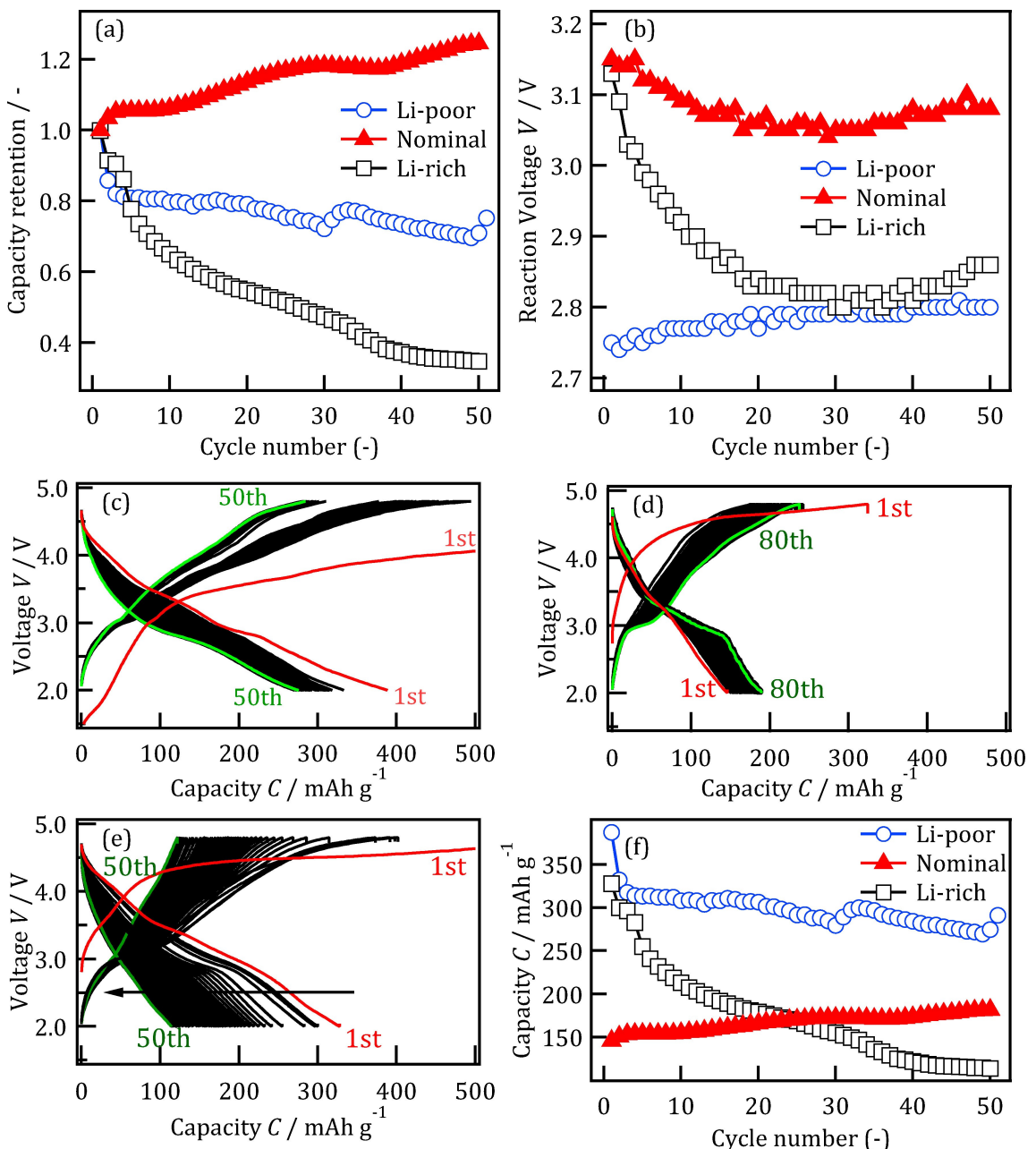


Figure 4. Cycle dependence of a) discharge capacities normalized by first discharge capacity and b) discharge reaction voltage of Li-poor, nominal, Li-rich $\text{Li}_x\text{Mn}_y\text{O}_{3-z}$ films ($\text{Li}/\text{Mn} = 1.75, 2.07$, and 2.28 , respectively) synthesized on $\text{SrRuO}_3/\text{SrTiO}_3(111)$ substrates. Charge-discharge curves of c) Li-poor, d) nominal, e) Li-rich $\text{Li}_x\text{Mn}_y\text{O}_{3-z}$ films ($\text{Li}/\text{Mn} = 1.75, 2.07$, and 2.28 , respectively). f) Cycle dependence of specific discharge capacities of all films. The data of the charge-discharge curves for Li-poor, nominal films, and cycling dependence for all the films were calculated from previous publication.^[11,17]

that activation happens over several cycles. In the subsequent cycles, both 001 and $\bar{2}02$ peaks shifted reversibly. The Li_2MnO_3 film transformed to a high-capacity phase associated with the structural reconstruction during the initial deintercalation and intercalation process. Figures 5c and 5d show the in-plane 060 and 020 peaks. The 060 peak shifted slightly from $d = 3.861$ to 3.864 then to 3.857 \AA during the first charge and discharge. In the subsequent cycles, the 060 peak also shifted reversibly with smaller changes than those observed for the 001 and $\bar{2}02$ peaks. In addition, no significant change was observed for the peak positions and intensities of the 060 peak during the

cycling, which might have been caused by a large constraint by the substrate lattice with large domain size. The above results suggest that an irreversible structural transition happened during the first cycle, resulting in shifting of the peaks between OCV and after the first discharge. Structural changes are reversible in the second and subsequent cycles. As there is no peak splitting, the activation is a gradual process where the entire film changes homogeneously.

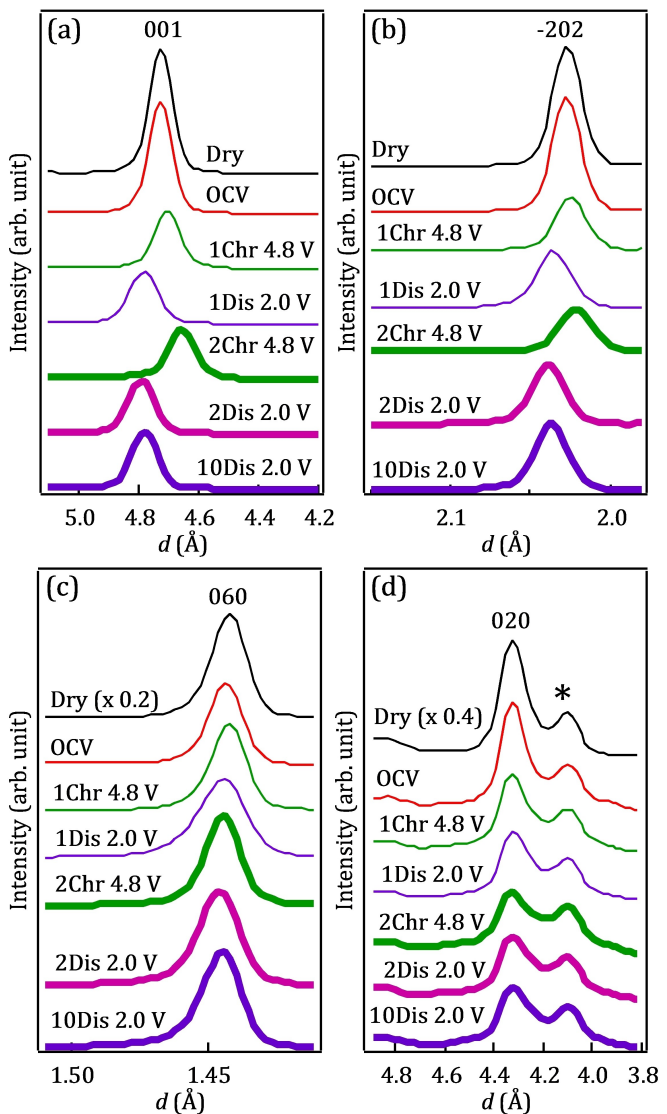


Figure 5. In situ XRD patterns showing the a) 001, b) $\bar{2}02$, c) 060, and d) 020 diffraction peaks of the nominal $\text{Li}_x\text{Mn}_y\text{O}_{3-z}$ (001) film electrode ($\text{Li}/\text{Mn}=2.07$) during electrochemical cycles: pristine state (Dry), after cell construction (OCV), charge (Chr.), and discharge (Dis.).

2.3.2. Li-Rich Film with $\text{Li}/\text{Mn}=2.28$ and Small Domain Size (20 nm)

Figures 6a and 6b show the 001 and $\bar{2}02$ peaks in the out-of-plane XRD patterns of the Li-rich film in the pristine state (Dry), after cell construction (OCV), after the first charge at 4.8 V, after the first discharge to 2.0 V, and during the subsequent cycles. After charging to 4.8 V, the 001 and $\bar{2}02$ peaks shifted to lower d values from 4.773 to 4.657 Å and from 2.029 to 2.012 Å, respectively, with a decrease in the intensities. These peak shifts in the Li-rich film were larger than those observed for the nominal film, indicating that the transition in the former is more significant than the latter. With the first discharge from 4.8 to 2.0 V, the 001 and $\bar{2}02$ peaks shift to higher d -values of 2.051 and 4.794 Å, respectively. This behavior is similar to those observed for the nominal film. Furthermore, the $\bar{2}02$ peak

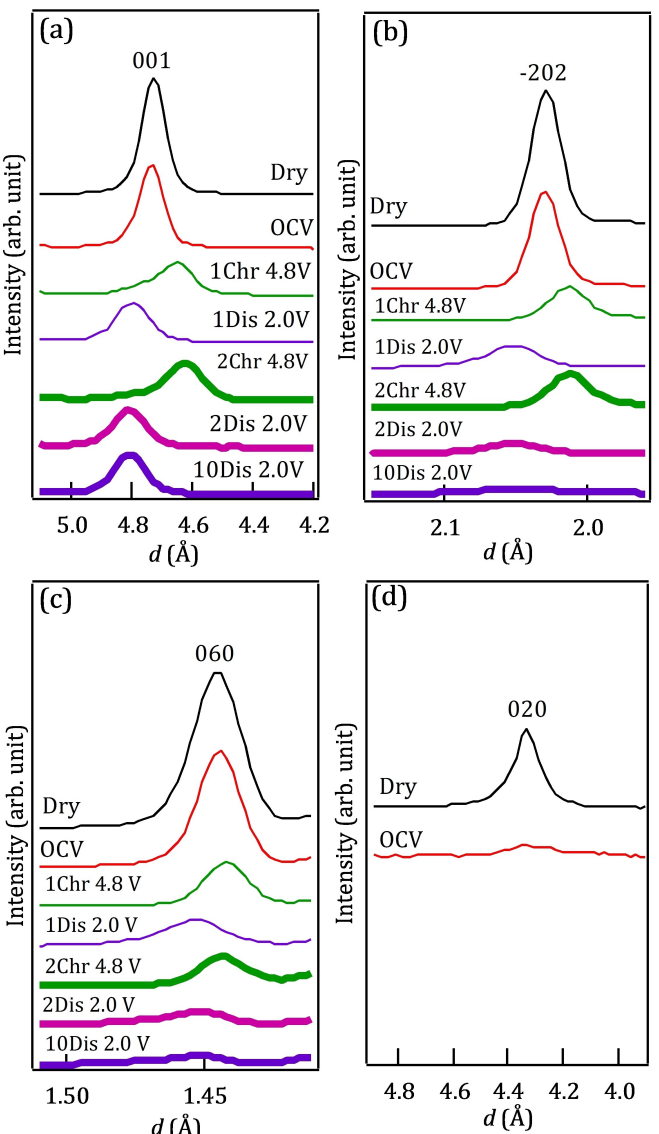


Figure 6. In situ XRD patterns showing the a) 001, b) $\bar{2}02$, c) 060, and d) 020 diffraction peaks of the Li-rich $\text{Li}_x\text{Mn}_y\text{O}_{3-z}$ (001) film electrode ($\text{Li}/\text{Mn}=2.28$) during electrochemical cycles (pristine state (Dry), after cell construction (OCV), charge (Chr.), and discharge (Dis.)).

intensities drastically decreased after the second cycle, which implies a structural degradation of the reconstructed phase at high voltage. Figures 8c and 8d show in-plane XRD patterns near 060 and 020 peaks. The 060 peak shifted from $d=1.443$ to 1.441 and then 1.444 Å during the first charge and discharge. The 020 peak was not observed after the cell construction, which is the first step leading to structural changes during cycling and is a phenomenon also observed in other layered cathode materials such as $\text{LiNi}_{0.8}\text{Co}_{0.2}\text{O}_2$.^[23] In Li_xMnO_3 , this observation implies introduction of stacking faults in the c -axis direction and/or disorder of Li, Mn, and vacancies in the transition metal layer.^[24] The shifts of the 060 peak were larger than those observed for the nominal film, and the peak intensity also gradually decreased after the second and tenth

cycles. These results reveal that the structural degradation of the active phase proceeded over many cycles.

2.4. Changes in Chemical Bonding State in First Charge–Discharge Cycle

2.4.1. Changes in Mn Valence

Figures 7a–7c show the Mn 3s core-level spectra of the Li-poor, nominal, and Li-rich films in the pristine state, after the first charge to 4.8 V, and after the first discharge to 2.0 V. The spectra for the Li-poor film in Figure 9a consist of four components with binding energies of 83.8, 84.0, 87.3, and 88.4 eV. The peaks at 83.8 and 87.3 eV are attributed to the 4f state of Au, which was used as the current collector. The peaks at 84 and 88 eV are attributed to the Mn 3 s state. The difference in peak positions (peak split) estimated by peak fitting using the Voigt function with two components was 4.4 eV for the pristine Li_2MnO_3 , which is consistent with 4.4 eV reported for the 4+ state.^[25] After the first charge to 4.8 V, the peak split increased to 5.0 eV, suggesting reduction of Mn to a lower valent state. After the first discharge to 2.0 V, no significant changes in the peak position and FWHM (full width at half maximum) values were observed, indicating that there were no changes in the oxidation state of Mn ions during the first discharge. The peak split for the pristine state was also 4.4 eV in the nominal and Li-rich films (Figure 7b and 7c, respectively). The peak split did not change during the first charge but increased to 4.9 eV during discharge in the nominal film. On the other hand, the peak split increased to 5.2 eV after first charge and further to 5.7 eV after first discharge in the Li-rich film. These results suggest that Mn is reduced regardless of the Li/Mn ratio, but the reduction process was completely different in the investigated three films.

2.4.2. Changes in O Valence

Figures 7d–7f show the O 1s spectra of the Li-poor, nominal, and Li-rich films, respectively, in the pristine state, after the first charge to 4.8 V, and after the first discharge to 2.0 V. In the Li-poor film, the pristine sample showed broad and well-defined peaks at binding energies of 532.4, 530.1, and 529.1 eV (see Figure 7d), which are assigned to carbonate species on the electrode surface, lattice O in $\text{Li}_4\text{Mn}_5\text{O}_{12}$ (spinel), and $\text{Li}_x\text{Mn}_y\text{O}_{3-z}$ (lattice O^{2-}), respectively.^[26] The presence of the $\text{Li}_4\text{Mn}_5\text{O}_{12}$ spinel is consistent with a previous report of the spinel phase existing in Li–Mn–O compounds with low Li/Mn atomic ratio.^[27] The peak fitting of the spectra after charging to 4.8 V was examined using a model consisting of four components: Li_2MnO_3 at 529.1 eV (lattice O^{2-}), $\text{Li}_4\text{Mn}_5\text{O}_{12}$ at 530.3 eV (spinel), deposited species from the electrolyte at 532.2 eV,^[28] and another component at 529.6 eV (lattice $\text{O}^{(2-a)-}$). The additional component at 529.6 eV can be explained by the presence of oxidative lattice-O species, thus is denoted as $\text{O}^{(2-a)-}$ where a is a positive number. For the discharged state at 2.0 V, the peaks

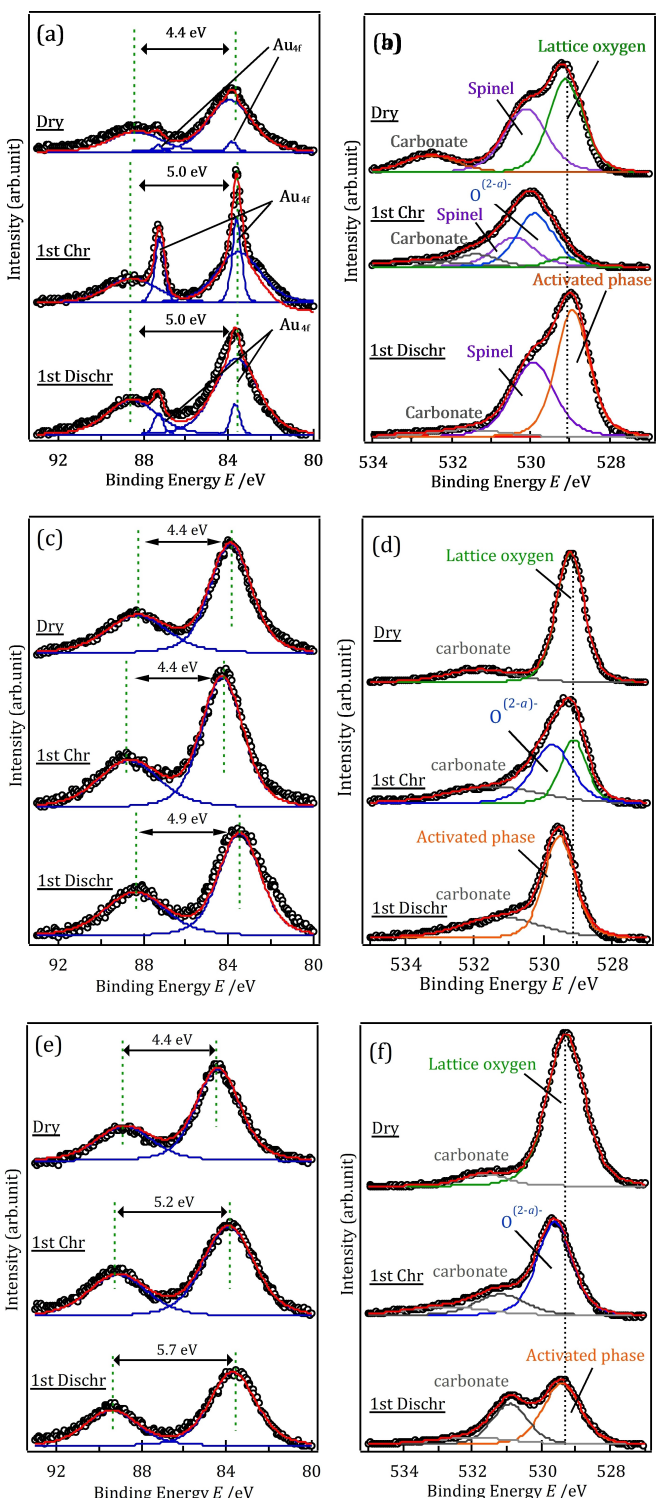


Figure 7. Mn 3 s and O 1s HAXPES spectra of a, b) Li-poor, c, d) nominal, and e, f) Li-rich $\text{Li}_x\text{Mn}_y\text{O}_{3-z}$ (001) film electrodes in the pristine state (Dry), after the first charge to 4.8 V (1st Chr), and after the first discharge to 2.0 V (1st Dischr).

are fitted by three components around 531.5, 530.0, and 528.9 eV, which correspond to the carbonates, $\text{Li}_4\text{Mn}_5\text{O}_{12}$ spinel, and $\text{Li}_x\text{Mn}_y\text{O}_{3-z}$ lattice O. The binding energy of 528.9 eV for the

peak corresponding to $\text{Li}_x\text{Mn}_y\text{O}_{3-z}$ lattice O^{2-} at 2.0 V was lower than the binding energy of 529 eV for the pristine state.

In the nominal film, similar peaks in the pristine film were observed around binding energies of 531.4 and 529.2 eV (see Figure 7e), which are assigned to lattice O in $\text{Li}_x\text{Mn}_y\text{O}_{3-z}$ and carbonate species on the electrode surface.^[26] After charging to 4.8 V, the binding energy increased, and the peak fitting using three components provided better fitting results. The three components are lattice O at 529.2 eV and deposited species at 531.6 eV,^[28] together with a new component at 529.8 eV ($\text{O}^{(2-a)-}$), which can be attributed to the presence of a lattice-O species with higher oxidation state. For the peak fittings of the spectrum of the film in the charged state, a two-peak model was used to fit the main peak, and both components are attributed to lattice O in $\text{Li}_x\text{Mn}_y\text{O}_{3-z}$. For the spectrum of the film in the discharged state at 2.0 V, the peaks were fitted by two components around 531.4 and 529.7 eV, which correspond to carbonates and lattice O. The binding energy of 529.5 eV for the peak corresponding to lattice O at 2.0 V was higher than the binding energy of 529 eV for the corresponding peak in the spectrum of the film in the pristine state. This indicates that the condition of O after discharge was different from that in the initial state. The small amount of carbonates and the suppression of a problematic side reaction, namely SEI formation, are factors that contribute to stable cycling with a low degree of degradation.

In the Li-rich film, the pristine film with $\text{Li}/\text{Mn}=2.28$, the peaks were observed around 531.7 and 529.3 eV (see Figure 9f), which correspond to lattice O and the carbonates, respectively. After charging to 4.8 V, the main peak shifted toward higher binding energies, and these peaks were fitted by the two components of lattice O at 529.6 eV and deposited species at 531.3 eV,^[28] together with a new component at 529.8 eV ($\text{O}^{(2-a)-}$). This additional component can be attributed to the presence of a lattice-O species with higher oxidation state, just like that in the film with $\text{Li}/\text{Mn}=2.07$. After discharging to 2.0 V, the peaks were also fitted by two components at 531.0 and 529.4 eV, which correspond to carbonates and lattice O.

The slight decrease in binding energy from 529.5 to 529.2 eV for lattice O with the discharge from 4.8 to 2.0 V indicates that O reduction took place. However, the discharged state had a slightly higher value than the original state, indicating a slightly higher oxidation state at 2.0 V than that of the pristine sample. Besides, carbonate species increased after the first cycle, indicating that organic electrolyte continued to decompose and form SEI layer on $\text{Li}_x\text{Mn}_y\text{O}_{3-z}$ film.

2.5. Summary of the Results

Table 3 provides a summary of the results; the composition of the thin films obtained primarily by ICP-MS analysis, lattice parameters, thickness, and roughness using XRD and XRR, and the domain size through TEM or AFM (section 2.1). The speed of transformation and degradation was deduced from the cycle dependence on capacity retention and reaction voltage (section 2.2), respectively. The transformation speed of normal and Li-rich films was also inferred from XRD results (section 2.3). The speed of change in Li/Mn ordering with cycling was obtained from changes in the 020 peak intensity (section 2.3). The change in valence with cycling was obtained from HAXPES measurements (section 2.4.1 and 2.4.2 for Mn and O, respectively). The Mn valence was quantified with the relation between Mn 3 s split and valence in Ref. [25]. No changes in the SEI with cycling was confirmed with HAXPES measurements (section 2.4.2).

3. Discussion

3.1. Activation Process and Cycling Stability

The electrochemical results are summarized as follows. (1) Nominal film with large domain size: after an irreversible structural change in the first cycle, activation proceeded slowly. (2) Li-rich film with small domain size: after an irreversible

Table 3. Summary of thin-film composition, structure, and electrochemical performance.

Sample	Li-poor	Nominal	Li-rich
Thin-film composition	Li/Mn atomic ratio	1.75	2.28
Structure	Lattice parameters	$a=4.941(2)$ Å $b=8.558(4)$ Å $c=5.010(8)$ Å $\beta=109.190(19)^\circ$	$a=4.946(9)$ Å $b=8.568(16)$ Å $c=5.037(6)$ Å $\beta=109.105(14)^\circ$
Changes with cycling	Thickness, t	25.0 nm	26.8 nm
	Roughness, r	1.7 nm	2.4 nm
	Domain size	5 nm	250 nm
	Transformation	Fast	Slow
	Degradation	None	Slow
Valence state	Li and Mn disordering	–	Slow
	Mn in pristine film	4+ (4.4 eV)	4+ (4.4 eV)
	Mn after first charge	3.3+ (5.0 eV)	4+ (4.4 eV)
	Mn after first discharge	3.3+ (5.0 eV)	3.4+ (4.9 eV)
	O in pristine film	O^{2-} (529.1 eV)	O^{2-} (529.2 eV)
	O after first charge	$\text{O}^{(2-a)-}/\text{O}^{2-}$ (529.6/529.1 eV)	$\text{O}^{(2-a)-}/\text{O}^{2-}$ (529.8/529.2 eV)
	O after first discharge	O^{2-} (528.9 eV)	O^{2-} (529.7 eV)
SEI	Carbonate intensity in HAXPES spectrum	No change	Increased

structural change in the first cycle, activation proceeded quickly. (3) Li-poor film with very small domain size: the activation process is as fast as that of the Li-rich film. However, whether a transition happened at the first cycle cannot be confirmed. The intrinsic reaction of the cathode material with cycling should be best reflected in the nominal film with large grain size: the ratio of the cathode material near the surface (surface region) to material far from the surface (bulk region) is large in small grains, thus reactions in the bulk regions are almost wiped out by those in the surface region in the observations. As a result, a two-step reaction mechanism is considered as the intrinsic reaction in Li_2MnO_3 . Interestingly, the very fast structural change in the first cycle is a bulk reaction that happens even in large grains. Although the details of the subsequent slow activation process cannot be precisely obtained from our current results, one hypothesis is minor rearrangements of atoms that eases Li diffusion in the transformed bulk. The slow degradation with cycling in the Li-poor film showed that the mixed-phase texture with $\text{Li}_x\text{Mn}_y\text{O}_{3-z}$ and $\text{Li}_4\text{Mn}_5\text{O}_{12}$ might have stabilized the activated phase during cycling, for example by inducing strain in $\text{Li}_x\text{Mn}_y\text{O}_{3-z}$, which is consistent with the stabilization of the layered cathode phase by spinel components.^[29,30] We also rule out the Li concentration dependence on the reaction mechanism; although the basic crystal framework is the same, the intrinsic reaction mechanism in Li-rich and Li-poor compositions may differ from almost stoichiometric Li_2MnO_3 .

Elucidation of the structural change during the activation process is a very intriguing topic. XRD results show that activation is accompanied by an increase in the interlayer distance. An implication is an increase in interatom distance, leading to faster in-plane Li diffusion. One possibility is transformation from the O3 structure to the O1 structure. Here out-of-plane Li diffusion is facilitated because Li layer and transition metal layer cation octahedra face share, thus, unlike the O3 structure, diffusion via a tetrahedral site is not necessary between these octahedra. Among the three films considered in this study, the nominal film provided most insights into the intrinsic reactions of Li_2MnO_3 during cycling because there was very little interaction with the SEI. However, the information obtained from the measurements was not sufficient to confirm further structural details on the activation process. Using an all-solid-state cell setup can eliminate the interactions between cathode and electrolyte and therefore eliminate the SEI.

3.2. Charge Compensation

The HAXPES O peak with binding energy near 529 eV at the HAXPES O 1s peak for lattice Li_xMnO_3 is a single peak. There is also a separate carbonate peak nearby in all films and a spinel $\text{Li}_4\text{Mn}_5\text{O}_{12}$ peak in the Li-poor film, which are not discussed here. An O component at higher binding energy, which typically means that the ion has further oxidized, appeared in the first charged state at 4.8 V for all films. The original O peak (s) still exist, although with a lower intensity, at first charge, therefore only some of the O are oxidized using the charged

species. The original peak slightly shifts to low binding energy in the Li-rich film, but the overall trend is the same among the three peaks. The exact charge cannot be deduced from the HAXPES results only, thus we denoted the species as $\text{O}^{(2-a)-}$ (a is a positive number) in Table 3. After discharge, the O peaks reverted to the original position in the Li-poor and Li-rich films. This result suggests, but does not absolutely confirm, that there was no large structural change in the first cycle. On the other hand, the main O peak clearly shifted to higher binding energy in the nominal film. Four drivers could cause this type of peak shift, which are structural transition, shift of the Fermi energy with respect to the band gap from, for instance, changes in the carrier type and/or concentration, charging (charge-up), and band bending. Structural changes and Fermi energy shift are consequences of changes in the bulk. Charge-up is unlikely because the electron is film and is coated with Au. In contrast, band bending is caused by modifications to the surface or interface, for instance by changes in the local coordination, for example by rearrangement of dangling bonds, or charge accumulation. As a consequence, the reason for the main O peak shift would be a structural change, which is implied from XRD results, and may be a shift in the Fermi energy or band bending.

On the other hand, the Mn valence changes were quite unusual. The split between two Mn 3s peaks is considered to be a measure of the Mn valence.^[25] Therefore, no change in the split between two Mn 3s peaks are anticipated because no valence changes in Mn from 4+ is expected by the electrochemical oxidation to 4.8 V. Interestingly, the Mn 3s peak split increased through cycling in all three films, suggesting a reduction of Mn through the cycling process. There is no splitting of individual Mn peaks, thus all Mn are considered to have the same valence. Very intriguingly, believing standard HAXPES theory leads to the conclusion that Mn reduces and O oxidizes simultaneously during charging, in Li-poor and Li-rich films. Moreover, the O valence does not change but Mn significantly reduces after cycling in Li-rich films. If the amount of Li removed during charge is not fully recovered during discharge, the atoms should be, on the whole, oxidized.

3.3. Surface Structure Changes

No significant intensity change in the HAXPES O 1s carbonate peak was observed in the nominal film, indicating the existence of carbonate components in the SEI layer formed after battery formation and these components remained during the charge-discharge reactions. In contrast, the carbonate peak in the Li-rich film gradually increased with cycling, indicating the growth of carbonate components on the Li_2MnO_3 surface during the charge and discharge. Dissolution of Mn to the electrolyte and forming a compound with reduced valence, for instance MnF_2 , is one possible explanation for reduction in the average valence of Mn, particularly in the Li-rich film with largest change in the Mn peak split and carbonate peak intensity. However, this hypothesis is rejected because there is no broadening in the Mn 3s peaks, indicating that all Mn has the same valence. One

may think that the smaller size of the Li-rich grains may have resulted in a larger surface region and thus can accelerate reaction with the SEI. In fact, Yabuuchi *et al.* examined the relative peak intensity of carbonate components nanoscale and macroscale Li_2MnO_3 with respect to that of oxide ions in nanoscale and microscale Li_2MnO_3 samples by XPS measurements. They found that the accumulation of carbonate species was much more intense in the nanoscale sample.^[31] However, the carbonate peak did not increase in the Li-poor film, rejecting this hypothesis. As a result, the increase in the carbonate peak in the Li-rich film should be ascribed to the Li-rich composition. We also note that the shift in the carbonate peak position does correlate with the Mn 3s peak split: the peak shifts to lower binding energy as the peak split increases. We therefore consider that HAXPES results are mostly governed by the region near the SEI layer, and that changes in the Mn 3s peak split should arise from changes in the local environment around Mn during charge and discharge because the Mn 3s peak split does not completely correlate with the valence. The observed changes in the valence during cycling may be affected by interactions with the SEI. Evaluating an all-solid-state cell would eliminate the influence from the SEI, therefore providing clearer insight into the intrinsic valence changes of Li_2MnO_3 with cycling.

4. Conclusions

Epitaxial film electrodes with 30 nm-thick $\text{Li}_x\text{Mn}_y\text{O}_{3-z}$ (001) layers of various Li concentrations using PLD under different synthesis conditions. These electrodes showed different degradation characteristics depending on the composition and morphology. The nominal (Li/Mn atomic ratio = 2.07) and Li-rich (Li/Mn ratio = 2.28) $\text{Li}_x\text{Mn}_y\text{O}_{3-z}$ films underwent irreversible structural transformation to an activated phase, regardless of the grain size, during cycling to 4.8 V. Further degradation was slower in the nominal film, but the reason cannot be clearly ascribed to composition or grain size. HAXPES results suggest that some O were reduced but others were not during charge. There were two types of O valences when charged to 4.8 V in all investigated films. Contrary to intuition, the increase in the Mn 3s peak split during cycling suggest that Mn is reduced during the cycling process in all films. However, there is no further evidence affirming Mn reduction. The Li-rich film shows large interactions with the SEI layer by virtue of the high Li concentration. Large grain size and not increasing the Li concentration above a certain threshold would enhance the performance of a Li_2MnO_3 cathode. Using an all-solid-state cell would provide further insights on the intrinsic behavior of Li_2MnO_3 because the effects of the SEI and other quirks resulting from the liquid electrolyte will be eliminated and further details on structural changes during the activation process may be available.

Acknowledgments

This work was supported by JSPS KAKENHI Grant Number JP 17H0614, the Research and Development Initiative for Scientific Innovation of New Generation Batteries (RISING2), JPNP16001, commissioned by the New Energy and Industrial Technology Development Organization (NEDO; Japan) and, Program on Open Innovation Platform with Enterprises, Research Institute and Academia (OPERA), JPMJOP1862, from the Japan Science and Technology Agency (JST). The synchrotron experiments were performed under the approval of the Japan Synchrotron Radiation Research Institute (JASRI) (Proposal Nos. 2016B1768, 2016A1675, 2015A3623, 2015A1574, 2015A1846, 2014B3623, 2014A1573, 2013B1530, 2013A3617, 2012A1615, and 2012B1286).

Conflict of Interest

The authors declare no conflict of interest.

Keywords: epitaxial thin-film · Li-rich materials · in-situ XRD · HAXPES · reaction mechanism

- [1] A. D. Robertson, P. G. Bruce, *Chem. Commun.* **2002**, 2790–2791.
- [2] K. Mizushima, P. C. Jones, P. J. Wiseman, J. B. Goodenough, *Mater. Res. Bull.* **1980**, *15*, 783–789.
- [3] N. Yabuuchi, T. Ohzuku, *J. Power Sources* **2003**, *119*–*121*, 171–174.
- [4] a) A. R. Armstrong, M. Holzapfel, P. Novák, C. S. Johnson, S.-H. Kang, M. M. Thackeray, P. G. Bruce, *J. Am. Chem. Soc.* **2006**, *128*, 8694–8698; b) Z. Lu, D. D. MacNeil, J. R. Dahn, *Electrochem. Solid-State Lett.* **2001**, *4*, A191–A194; c) N. Yabuuchi, K. Yoshii, S.-T. Myung, I. Nakai, S. Komaba, *J. Am. Chem. Soc.* **2011**, *133*, 4404–4419.
- [5] M. Balasubramanian, J. McBreen, I. J. Davidson, P. S. Whitfield, I. Kargina *J. Electrochem. Soc.* **2002**, *149*, A176–A184.
- [6] a) J. Rana, M. Stan, R. Kloepsch, J. Li, G. Schumacher, E. Welter, I. Zizak, J. Banhart, M. Winter, *Adv. Energy Mater.* **2014**, *4*, 1300998–1300912; b) A. D. Robertson, P. G. Bruce, *Chem. Mater.* **2003**, *15*, 1984–1992.
- [7] J.-S. Kim, C. S. Johnson, J. T. Vaughey, M. M. Thackeray, S. A. Hackney, W. Yoon, C. P. Grey, *Chem. Mater.* **2004**, *16*, 1996–2006.
- [8] M. Sathiya, G. Rousse, K. Ramesha, C. P. Laisa, H. Vezin, M. T. Sougrati, M. L. Doublet, D. Foix, D. Gonzeau, W. Walker, A. S. Prakash, M. Ben Hassine, L. Dupont, J. M. Tarascon, *Nat. Mater.* **2013**, *12*, 827–835.
- [9] a) M. Cheng, W. Tang, Y. Li, K. Zhu, *Catal. Today* **2016**, *274*, 116–122; b) A. Klein, P. Axmann, C. Yada, M. Wohlfahrt-Mehrens, *J. Power Sources* **2015**, *288*, 302–307; c) S. F. Amalraj, L. Burlaka, C. M. Julien, A. Mauger, D. Kovacheva, M. Taliander, B. Markovsky, D. Aurbach, *Electrochim. Acta* **2014**, *123*, 395–404.
- [10] a) M. Hirayama, N. Sonoyama, T. Abe, M. Minoura, M. Ito, D. Mori, A. Yamada, R. Kanno, T. Terashima, M. Takano, K. Tamura, J. Mizuki, *J. Power Sources* **2007**, *168*, 493–500; b) M. Hirayama, H. Ido, K. Kim, W. Cho, K. Tamura, J. I. Mizuki, R. Kanno, *J. Am. Chem. Soc.* **2010**, *132*, 15268–15276.
- [11] S. Taminato, M. Hirayama, K. Suzuki, N. L. Yamada, M. Yonemura, J. Y. Son, R. Kanno, *Chem. Commun. (Camb.)* **2015**, *51*, 1673–1676.
- [12] K. Suzuki, K. Kim, S. Taminato, M. Hirayama, R. Kanno, *J. Power Sources* **2013**, *226*, 340–345.
- [13] G. M. Meyer, R. J. Nelmes, J. Hutton, *Ferroelectrics* **1978**, *21*, 461–462.
- [14] L. G. Parratt, *Phys. Rev.* **1954**, *95*, 359.
- [15] B. M. Ocko, J. Wang, A. Davenport, H. Isaacs, *Phys. Rev. Lett.* **1990**, *65*, 1466–1469.
- [16] B. Philippe, M. Hahlin, K. Edstrom, T. Gustafsson, H. Siegbahn, H. Rensmo, *J. Electrochem. Soc.* **2015**, *163*, A178–A191.
- [17] Y. Sugawara, S. Taminato, T. Hirayama, M. Hirayama, R. Kanno, Y. Ukyo, Y. Ikuhara, *J. Electrochem. Soc.* **2018**, *165*, A55–A60.
- [18] Y. S. Meng, G. Ceder, C. P. Grey, W. S. Yoon, M. Jiang, J. Bréger, Y. Shao-Horn, *Chem. Mater.* **2005**, *17*, 2386–2394.

- [19] V. Massarotti, M. Bini, D. Capsoni, A. Altomare, A. G. G. Moliterni, *J. Appl. Crystallogr.* **1997**, *30*, 123–127.
- [20] F. Massel, K. Hikima, H. Rensmo, K. Suzuki, M. Hirayama, C. Xu, R. Younesi, Y.-S. Liu, J. Guo, R. Kanno, M. Hahlin, L.-C. Duda, *J. Phys. Chem. C* **2019**, *123*, 28519–28526.
- [21] K. Hikima, K. Suzuki, S. Taminato, M. Hirayama, S. Yasuno, R. Kanno, *Chem. Lett.* **2019**, *48*, 192–195.
- [22] a) Z. Chen, Z. Lu, J. R. Dahn, *J. Electrochem. Soc.* **2002**, *149*, A1604; b) E. Levi, M. D. Levi, G. Salitra, D. Aurbach, R. Oesten, U. Heider, L. Heider, *Solid State Ionics* **1999**, *126*, 97–108; c) W. Li, J. N. Reimers, J. R. Dahn, *Solid State Ionics* **1993**, *67*, 123–130.
- [23] K. Sakamoto, M. Hirayama, N. Sonoyama, D. Mori, A. Yamada, K. Tamura, J. I. Mizuki, R. Kanno, *Chem. Mater.* **2009**, *21*, 2632–2640.
- [24] K. Hikima, Y. Hinuma, K. Shimizu, K. Suzuki, S. Taminato, M. Hirayama, T. Masuda, K. Tamura, R. Kanno, **2020**, submitted for publication.
- [25] V. Galakhov, M. Demeter, S. Bartkowski, M. Neumann, N. Ovechkina, E. Kurmaev, N. Lobachevskaya, Y. Mukovskii, J. Mitchell, D. Ederer, *Phys. Rev. B* **2002**, *65*, 113102.
- [26] J.-C. Dupin, D. Gonbeau, P. Vinatier, A. Levasseur, *Phys. Chem. Chem. Phys.* **2000**, *2*, 1319–1324.
- [27] D. Y. W. Yu, K. Yanagida, *J. Electrochem. Soc.* **2011**, *158*, A1015.
- [28] R. Dedryvère, D. Foix, S. Franger, S. Patoux, L. Daniel, D. Gonbeau, *J. Phys. Chem. C* **2010**, *114*, 10999–11008.
- [29] C. S. Johnson, N. Li, J. T. Vaughney, S. A. Hackney, M. M. Thackeray, *Electrochem. Commun.* **2005**, *7*, 528–536.
- [30] J. Cabana, S.-H. Kang, C. S. Johnson, M. M. Thackeray, C. P. Grey, *J. Electrochem. Soc.* **2009**, *156*.
- [31] N. Yabuuchi, K. Kubota, Y. Aoki, S. Komaba, *J. Phys. Chem. C* **2016**, *120*, 875–885.

Manuscript received: October 26, 2020

Revised manuscript received: November 11, 2020

Accepted manuscript online: November 17, 2020

Version of record online: December 10, 2020